ACS NANO

www.acsnano.org

ARTICLE

Conformational Dynamics of Influenza A Virus Ribonucleoprotein Complexes during RNA Synthesis

Diego Carlero,[¶] Shingo Fukuda,[*,¶] Rebeca Bocanegra,[¶] Toshio Ando, Jaime Martin-Benito,[*] and Borja Ibarra[*]

Cite This: *ACS Nano* 2024, 18, 19518–19527

Read Online

ACCESS | Metrics & More | Article Recommendations | Supporting Information

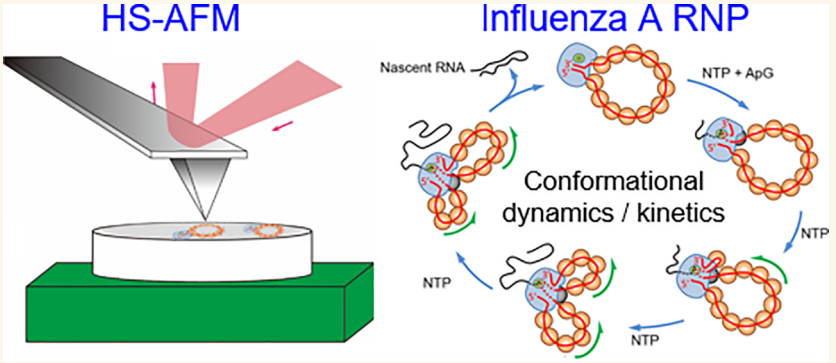

ABSTRACT: **Viral ribonucleoproteins (vRNPs) are the cornerstones of viral proliferation, as they form the macromolecular complexes that are responsible for the transcription and replication of most single-stranded RNA viruses. The influenza A virus (IAV) polymerase catalyzes RNA synthesis within the context of vRNPs where genomic viral RNA (vRNA) is packaged by the viral nucleoprotein (NP). We used high-speed atomic force microscopy and electron microscopy to study the conformational dynamics of individual IAV recombinant RNPs (rRNPs) during RNA synthesis. The rRNPs present an annular organization that allows for the real-time tracking of conformational changes in the NP-vRNA template caused by the advancing polymerase. We demonstrate that the rRNPs undergo a well-defined conformational cycle during RNA synthesis, which can be interpreted in light of previous transcription models. We also present initial estimations of the average RNA synthesis rate in the rRNP and its dependence on the nucleotide concentration and stability of the nascent RNA secondary structures. Furthermore, we provide evidence that rRNPs can perform consecutive cycles of RNA synthesis, accounting for their ability to recycle and generate multiple copies of RNA.**

KEYWORDS: *Influenza A virus, RNA synthesis, Conformational dynamics, High-speed atomic force microscopy, Electron microscopy, Single-molecule biophysics*

Influenza A virus (IAV) is a global public health threat that is responsible for seasonal epidemics and occasional pandemics of respiratory disease that cause substantial morbidity and mortality in humans. The viral genome consists of eight different segments of single-stranded, negative-polarity RNA (vRNA) assembled into viral ribonucleoprotein complexes (vRNPs).[1−5] The vRNP is the functional context in which the viral RNA-dependent RNA polymerase (RdRp) transcribes and replicates the vRNA.[6] Within each vRNP, partially complementary ends of the vRNA associate with RdRp to form the promoter for RNA synthesis.[7,8] The rest of the vRNA is bound to multiple copies of a nucleoprotein (NP), with a stoichiometry of approximately 24 bases per monomer.[9] Each vRNP adopts an antiparallel double-helical structure with the RdRp at one end and an NP loop structure at the other.[2,4] Recent biochemical and cryogenic electron

Received: January 29, 2024
Revised: May 13, 2024
Accepted: May 22, 2024
Published: July 16, 2024

https://doi.org/10.1021/acsnano.4c01362
ACS Nano 2024, 18, 19518−19527

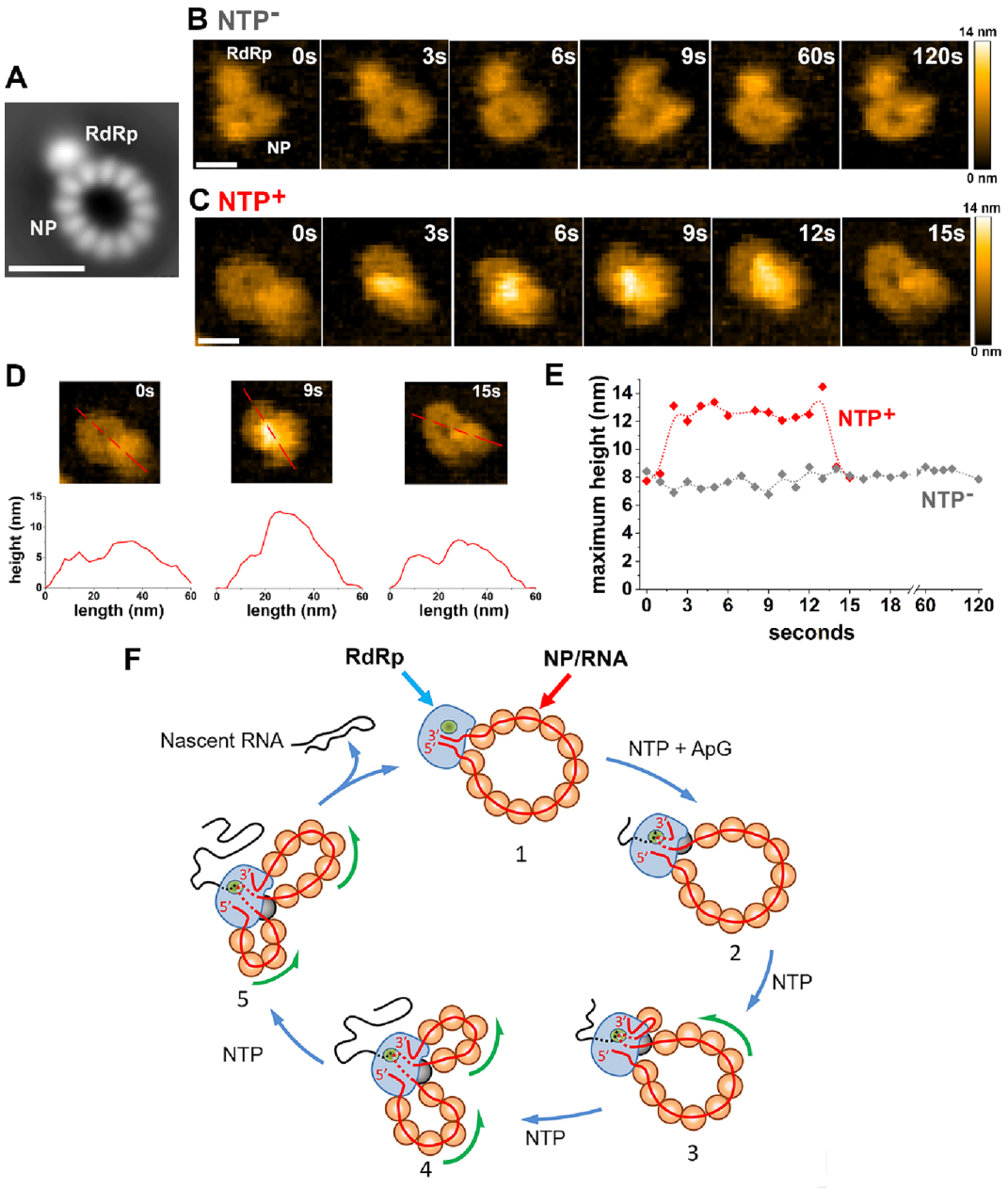

Figure 1. Visualization of conformational cycles of individual rRNPs during RNA synthesis. (A) 2D average of EM images of individual rRNPs showing their annular organization and the relative positions of the RdRp and NP/RNA template (number of images = 3648; scale bar = 20 nm). (B) Successive HS-AFM video frames of a single rRNP in the reaction buffer without NTPs, Supplementary Video 1 [2 frames/sec (fps)]. The RdRp and the NP/RNA template are clearly discernible. The rRNP preserves its structural organization and height profile after scanning times longer than 100 s (scale bar = 20 nm). Additional HS-AFM videos in the absence of NTPs are shown in Supplementary Video 2. C) Successive HS-AFM video frames of a single rRNP in the reaction buffer containing NTPs (100 μM) and ApG primer (100 μM), Supplementary Video 3 (1 fps). Under these conditions, the rRNP rapidly loses its annular organization and goes through conformational transitions before returning to its initial conformation. (D) Height profiles of frames 0, 9, and 15 s from C. Red lines indicate the axis on which the height measurements were taken. (E) Temporal evolution of the maximum height of the representative rRNP complex shown in C (red dots, Supplementary Video 3). Gray dots show the variation of the maximum height of the rRNP shown in panel B. Additional HS-AFM videos in the presence of NTPs are shown in Supplementary Videos 5−8. (F) Schematic diagram of the conformational cycle of rRNPs during RNA synthesis. (1) The rRNA template (red) is pseudo-circularized by promoter binding to the RdRp (blue) with the rest of the RNA forming a ring coated by NP (orange spheres); the RdRp active site is shown in green. (2) In the presence of NTP/ApG, the advancement of the RdRp during polymerization peels off the NP from the vRNA template, while the 3′ end of the template docks into a secondary binding site on the RdRp, where it remains bound until the end of the RNA synthesis cycle.[11] Local transient interactions between the peeled NP (gray sphere) and the RdRp would help to hold the NP in place for rebinding to the outgoing ssRNA template. (3) to (5) As the template is progressively translocated through the RdRp active site, the nascent RNA (black) grows and NP/RNA template loops are formed on both sides of the polymerase. The incoming loop shrinks while the outgoing loop grows as RNA synthesis proceeds. (5) to (1) Upon reading the full template and the concomitant disappearance of the incoming loop, the rRNP recovers its initial annular organization. Green arrows indicate the direction of template movement relative to the position of the RdRp. Supplementary Animation 1 presents a visualization of the proposed conformational cycle.

https://doi.org/10.1021/acsnano.4c01362
ACS Nano 2024, 18, 19518−19527

microscopy (cryo-EM) structural studies revealed that native vRNPs maintain their overall structures during the RNA synthesis cycle. This ability was attributed to highly dynamic vRNP interstrand interactions, in which the sliding of opposite strands allows the polymerase to access the entire RNA template while still binding to both 5′ and 3′ termini.[5] Additionally, the outgoing vRNA template would adopt a structure similar to the original superhelical genome segment. In this way, after synthesis of the full-length RNA template, the structure of the vRNP would be identical to the initial one, allowing the RdRp to initiate a new RNA synthesis cycle and generate multiple transcripts from a single vRNP. Despite the vRNP maintaining its overall structure during RNA synthesis, recent X-ray and cryo-EM structural studies of isolated actively transcribing RdRp from IAV and influenza B virus suggested that the topological constraint imposed by binding at both ends of the template would imply significant local restructuring of the NP-RNA strand at the polymerase location.[10,11] As the RdRp pulls the template vRNA from the NP into its active site during elongation, the outgoing template protrudes to form a growing loop, while the incoming template loop would simultaneously shrink. However, the bulky double-helical structure of the vRNPs prevented the detection of such putative local conformational changes in template directionality and hindered the precise localization of the RdRp position within the complex without labeling.

Considerable effort has been made to understand the structure and biochemical properties from isolated IAV RdRp.[10−14] However, these studies have provided snapshots of the highly dynamic process of RNA synthesis and outside its physiological context, the vRNP. Understanding the structural dynamics of vRNPs during RNA synthesis is essential to elucidating the real-time kinetic and morphological mechanisms underlying viral transcription and replication reactions. Here, we aimed to address these knowledge gaps by visualizing the structural dynamics of individual recombinant RNPs (rRNPs) during RNA synthesis using high-speed atomic force microscopy (HS-AFM). This technique allows for real-time observation of single biomolecules at 2−3 nm lateral and ∼0.1 nm vertical spatial resolutions under near physiological conditions without chemical labeling.[15−20] We used rRNPs that bear the same protein components as native vRNPs, but contain an RNA segment only 352 nt in length, which was previously shown to prevent supercoiling of NPs.[9] Instead, individual rRNPs presented a characteristic annular organization, in which the RdRp could be clearly differentiated from the NP-vRNA template.[21,22] HS-AFM videos revealed conformational changes in individual rRNPs during RNA synthesis in real time. Backed by EM imaging, our results showed that during RNA synthesis individual rRNPs undergo a well-defined conformational cycle that could be interpreted in light of previous RNA synthesis models. In addition, we showed evidence that rRNPs can perform several consecutive cycles of RNA synthesis, accounting for their predicted ability to recycle and generate multiple copies of mRNA. Finally, we provide estimations of the average RNA synthesis rate within the rRNP and its dependence on the NTP concentration and stability of nascent RNA secondary structures.

RESULTS AND DISCUSSION

HS-AFM Imaging Reveals Conformational Dynamics of rRNPs under Conditions Competent for RNA Synthesis. rRNPs were generated by *in vivo* amplification using cDNAs of the three polymerase subunits, the NP, and a model vRNA-like genome of 352 nt[9] (Experimental Section and Figure S1A). Different fractions from the purified rRNPs were assayed for *in vitro* transcriptional activity (Figure S1B). Initially, preparations of transcriptionally active rRNPs were visualized by negative staining EM and HS-AFM under conditions not compatible with RNA synthesis, i.e., in the absence of NTPs and ApG as a primer (Figure 1; Experimental Section). Classification and 2D averaging of the EM images showed that the rRNPs present annular shapes with the majority containing 12 NP monomers and a prominent mass at the external side of the NP ring consistent with the presence of the RdRp (Figures 1A and S1C). This organization is comparable to that of rRNPs with similar vRNA-like genome lengths studied previously.[9,21−23] Similarly, HS-AFM images of rRNPs deposited on bare mica also showed well-defined annular shapes with a protruding volume of the RdRp and dimensions compatible with those measured in EM images (Figures 1B and S2). These images contrast with those of full-length vRNPs where the double-helical structure of the complex impedes localization of the RdRp (Figure S2). In the absence of NTPs/ApG, the rRNPs maintained their overall organization during the entire observation time and showed only small distortions due to thermal agitation (Figure 1B, Supplementary Videos 1 and 2). Topographic images provided by HS-AFM showed average heights for the RdRp and the NP-RNA template of 8 ± 1 and 6 ± 1 nm, respectively. These heights are consistent with those obtained from the volumes of the three-dimensional reconstruction of rRNPs bearing ssRNA templates with similar lengths[22] and the crystal structure of IAV RdRp.[12,24]

Next, we aimed to investigate the conformational dynamics of the rRNPs under conditions compatible with RNA synthesis in the presence of the four NTPs (100 μM) and the dinucleotide ApG (100 μM) to prime RNA synthesis[25,26] (Experimental Section). Under these conditions, HS-AFM imaging revealed that some rRNPs lost their annular organization quickly and went through conformational transitions before returning to the original annular shape (Figure 1C and Supplementary Video 3). During these conformational transitions, the positions of the RdRp and the NP ring were no longer discernible. Instead, the height of the rRNP nearly doubled locally before returning to its initial values (Figure 1D and E). This local increase in height (13 ± 1 nm) is compatible with superimposition of the RdRp and one NP monomer. We consistently observed this behavior across N = 10 independent rRNPs (Supplementary Table S1). As described before, none of these conformational changes and height variations were observed in the absence of NTP/ApG (Figure 1B and E). These results strongly suggest that these conformational changes are associated with the RNA synthesis reaction by the RdRp within the rRNP context. Based on these and the results described below, Figure 1F and Supplementary Animation 1 depict schematic representations of the relative motion of the RdRp and NP/RNA template during RNA synthesis.

Conformational Transitions of rRNPs Correlate with RNA Synthesis. To confirm that the conformational transitions of the rRNPs in the presence of NTP/ApG are linked to RNA synthesis, we first measured the consequences on the conformational dynamics of rRNPs of stopping RNA synthesis once it has started. In this case, HS-AFM experiments were performed in a reaction buffer containing ApG (100 μM)

https://doi.org/10.1021/acsnano.4c01362
ACS Nano 2024, 18, 19518−19527

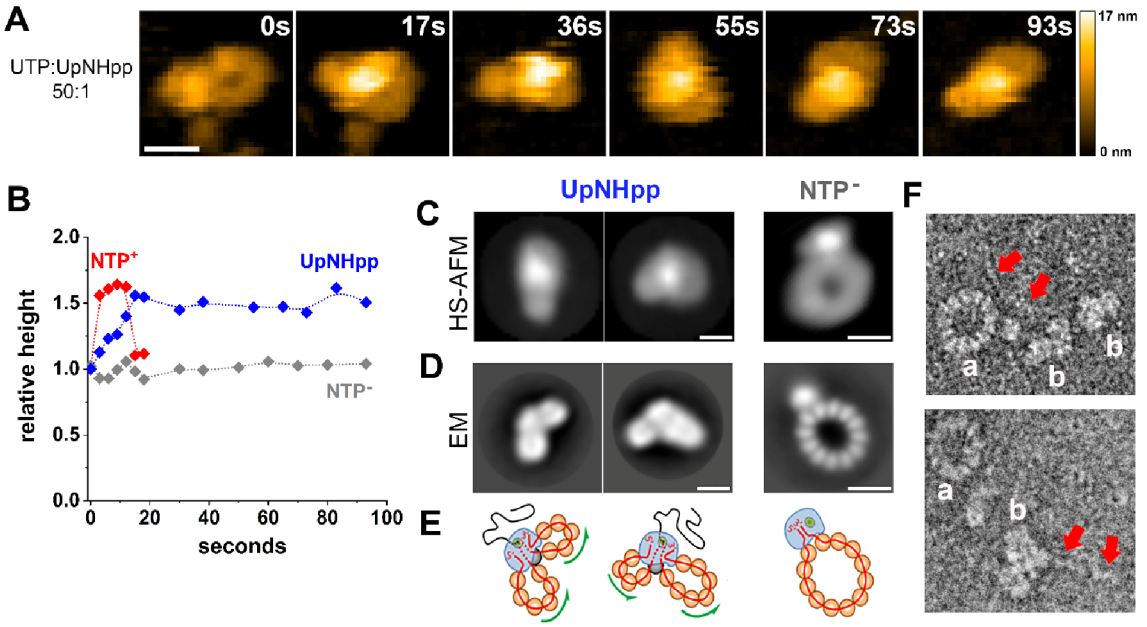

Figure 2. Correlation between conformational transitions of rRNPs and RNA synthesis. Interference of RNA synthesis by nonhydrolyzable UTP analog UpNHpp prevents the rRNP from recovering its initial annular organization and stalls conformational states with a local height increased. (A) Successive HS-AFM video frames of a single rRNP in the reaction buffer containing ApG (100 μM) and an NTP mixture (100 μM) including the nonhydrolyzable UpNHpp (2 μM), Supplementary Video 4 (2 fps); scale bar = 20 nm. (B) Variation of the relative maximum height over time in the presence of UpNHpp for the rRNP shown in A (blue dots, Supplementary Video 4). For comparison, gray and red symbols show the changes in time of relative maximum heights in the absence and presence of the four natural NTPs, respectively (as shown in Figure 1E). (C) Left panels show the 2D averages of HS-AFM frames of the major conformational states observed in the presence of UpNHpp (N = 60 and 62, first and second panel, respectively). Images were taken from two independent movies. Panel on the right shows the 2D average of HS-AFM frames of rRNPs in the absence of NTPs (N = 168). (D) Left panels show the 2D averages of EM images (N = 3414 and 2576, respectively) of major conformational states observed in the presence of UpNHpp. The panel on the right shows the 2D average of EM images of annular rRNPs in the absence of NTPs (as shown in Figure 1A). In C and D scale bars = 15 nm. (E) Diagrams depicting the corresponding conformational states of the rRNPs (as shown in Figure 1F). (F) EM images of rRNPs upon incubation in a reaction buffer competent for RNA synthesis containing UpNHpp (Experimental Section). Annular rRNPs (a) and rRNPs in compacted conformational states (b) can be observed. Red arrows show the position of fibers and other structures associated with the compacted rRNPs. None of these structures were observed in the absence of NTPs and are compatible with ssRNA synthesized during rRNP activity.

as primer and a mixture of the four NTPs (100 μM) including the nonhydrolyzable UTP analogue UpNHpp (2 μM). Under these conditions RNA synthesis would start normally, but the eventual competitive binding of UpNHpp will pause the synthesis reaction[11] and, consequently, also halt the conformational transitions. In these assays, HS-AFM imaging showed that the rRNPs initially undergo the same shape and height changes; however, the complexes never recover the original height and ring structure even if the observation time is prolonged (N = 3), Figure 2A and B, Supplementary Video 4. To visualize the rRNP in more detail, we performed 2D classification of the HS-AFM movie frames. This processing helps to mitigate the effects of lateral diffusion and drift observed during HS-AFM imaging. The 2D averages revealed an accumulation of elongated, bow-tie-like structures with an internal prominent bulge with an average height of 15 ± 1 nm (Figure 2C). These heights and morphologies were indistinguishable from those observed during the conformational transitions of the rRNPs in reactions run without UpNHpp. Overall, these results indicate that interference with RNA synthesis indeed arrests the conformational dynamics of the rRNP, showing the interdependence of these two processes.

The nascent single-stranded RNA associated with rRNPs during conformational transitions cannot be visualized with the current spatial resolution of HS-AFM. Thus, to visualize the nascent RNA synthesized by the rRNPs, we resorted to EM imaging. For these experiments, RNA synthesis reactions were started in the bulk in the presence of the ApG primer and NTP mixtures with UpNHpp (Experimental Section). After defined incubation times, the rRNPs were adsorbed on carbon-coated grids and imaged by negative staining EM (Experimental Section). Under these conditions, we observed the accumulation of elongated, compact complexes clearly discernible from the characteristic annular shape of the rRNPs not engaged in RNA synthesis. Classification and 2D averaging of these images revealed they present shapes and sizes compatible with those obtained from 2D averaging of individual HS-AFM frames (Figure 2D). In this case, the higher spatial resolution of EM clearly identified a bowtie-like organization of the arrested complexes, which presented two well-defined loops flanking a central density (Figure 2D). The relative sizes of the loops may reflect rRNPs at different stages of the elongation phase of RNA synthesis (Figure 2E). Importantly, in independent EM images, it was possible to clearly identify protruding filaments associated with the bowtie-like rRNPs (Figure 2F). These filaments were never observed in rRNP samples assayed under conditions not compatible with RNA synthesis. The filaments presented a width compatible with that of ssRNA visualized by negative staining EM and exhibited an overall morphology identical to that of ssRNA associated

https://doi.org/10.1021/acsnano.4c01362
ACS Nano 2024, 18, 19518−19527

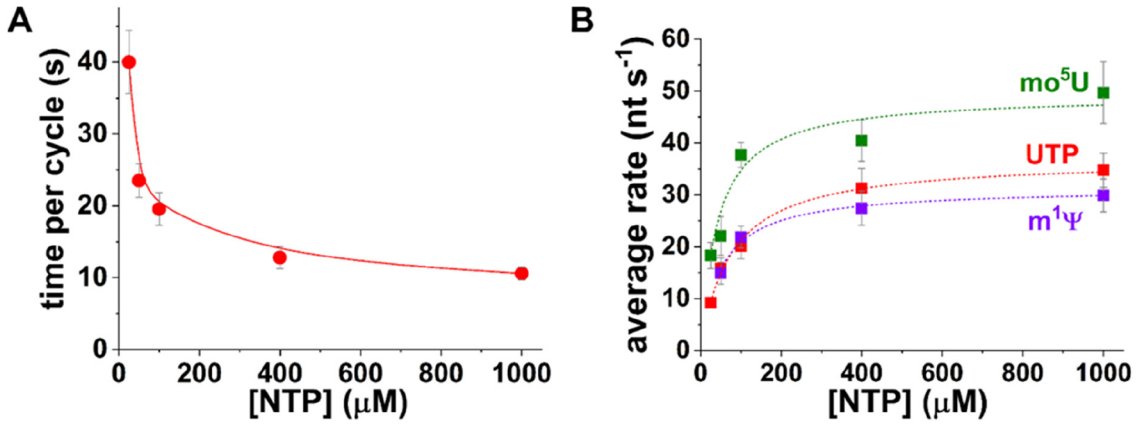

Figure 3. RNA synthesis rate is modulated by NTP concentration and stability of nascent RNA secondary structures. (A) Average duration of the conformational transitions between consecutive annular shapes as a function of NTP concentration (Supplementary Videos 5−8). (B) Variation of the average RNA synthesis rates with increasing concentrations of a mixture containing the four natural NTPs (labeled as UTP, red) or methyl-pseudouridine ($m^1\Psi$, purple) or 5-methoxy-uridine (mo^5U, green) instead of UTP. mo^5U promotes less stable secondary structures on ssRNA than $m^1\Psi$ and UTP. In A and B lines serve as visual guides. The error bars represent the standard error of the mean. Supplementary Table S1 lists the number of active, independent rRNPs measured for each condition. Supplementary Videos 9 and 10 show HS-AFM videos taken in the presence mo^5U and $m^1\Psi$, respectively.

with actively transcribing native vRNPs studied previously by EM.[5] Note that the flexibility of the nascent ssRNA impedes its visualization in the 2D average images of the arrested conformations. This evidence strongly suggests that the filaments associated with the arrested, bowtie-like compact rRNPs may correspond to the nascent ssRNA, supporting a direct link between the conformational transitions of the rRNP and RNA synthesis.

RNA Synthesis Rate Is Modulated by NTP Concentration and the Stability of the Nascent RNA Secondary Structure. According to the above results, there is a direct link between the conformational transitions observed by HS-AFM and RNA synthesis. As described for other RNA polymerases,[27−29] the average RNA synthesis rate of the IAV RdRp is expected to depend on NTP concentration. Therefore, it follows that the average time it takes for an individual rRNP to go through a full conformational cycle (defined as all of the transitions between two consecutive annular shapes) should also depend on the NTP concentration. We aimed to check this possibility by measuring the average conformational cycle duration of individual rRNPs at increasing NTP concentrations from 25 to 1000 μM and with ApG at 100 μM (Supplementary Videos 5−8). Supplementary Table S1 lists the number of active, independent rRNPs measured for each condition. The time to accomplish a full cycle decreased gradually as the NTP concentration increased, reaching saturation at concentrations above ∼400 μM (Figure 3A). These results further support the correlation between the cycle of conformational changes and the synthesis of nascent RNA. Since rRNPs present a template with a well-defined length, the average rate of RNA synthesis can be estimated by dividing the number of template nucleotides (352 nt) by the time required to complete a single conformational cycle. As expected, the average RNA synthesis rate increased sigmoidally until saturation at 400 μM NTP with a value of 31 ± 4 nt/s, Figure 3B.

Several lines of evidence in bacterial and eukaryotic RNA polymerases have shown that secondary structure within the nascent RNA chain regulates average transcription rates.[29−32] According to UNAfold secondary structure predictions,[33] the nascent RNA leaving the rRNP can form stable secondary structures (Figure S3). To determine the effect of nascent RNA secondary structure stability on the average RNA synthesis rate, we measured the time for individual rRNPs to undergo a conformational cycle in the presence of increasing NTP concentrations, where UTP was replaced by N^1-methyl-pseudouridine ($m^1\Psi$) or 5-methoxy-uridine (mo^5U). Although these two UTP analogs maintain the same Watson−Crick base pairing relationships, $m^1\Psi$ increases while mo^5U decreases base pairing stability.[34] Neither of these analogs significantly affected *in vitro* RNA synthesis by the rRNPs (Figure S1B). HS-AFM imaging revealed that incorporation of $m^1\Psi$ slowed down the average rate slightly with respect to control UTP conditions, an effect mainly observed at saturating NTP concentrations (Figure 3B, Supplementary Video 9). Interestingly, mo^5U had a more noticeable effect; at all NTP concentrations this analog increased the average RNA synthesis rate by 1.5 to 2 times with respect to control UTP conditions (Figure 3B, Supplementary Video 10). These results strongly suggest that the stability of the secondary structure of the nascent RNA regulates the activity of the IAV RdRp within the context of the RNP. In particular, nascent RNAs with weaker secondary structures would favor the average synthesis rate of the polymerase.

Consecutive Cycles of RNA Synthesis by Individual rRNPs. Under conditions that favored RNA synthesis, HS-AFM imaging revealed that a significant number of rRNPs (∼16% of the active rRNPs imaged in this study) went through consecutive conformational cycles (Supplementary Videos 11 and 12, Figure 4A). In other words, upon finishing a conformational cycle and recovering their initial height, these rRNPs again proceeded through one or more similar conformational transitions (Figure 4B). Notably, the times to complete each conformational cycle were similar to those measured for rRNPs that underwent only a single cycle, and they presented an identical dependence on NTP concentration (Figure 4C). These results further support that a full conformational cycle would correspond to the processing of the full template, which in turn, validates our estimations of the average RNA synthesis rates. In addition, these results provide

https://doi.org/10.1021/acsnano.4c01362
ACS Nano 2024, 18, 19518−19527

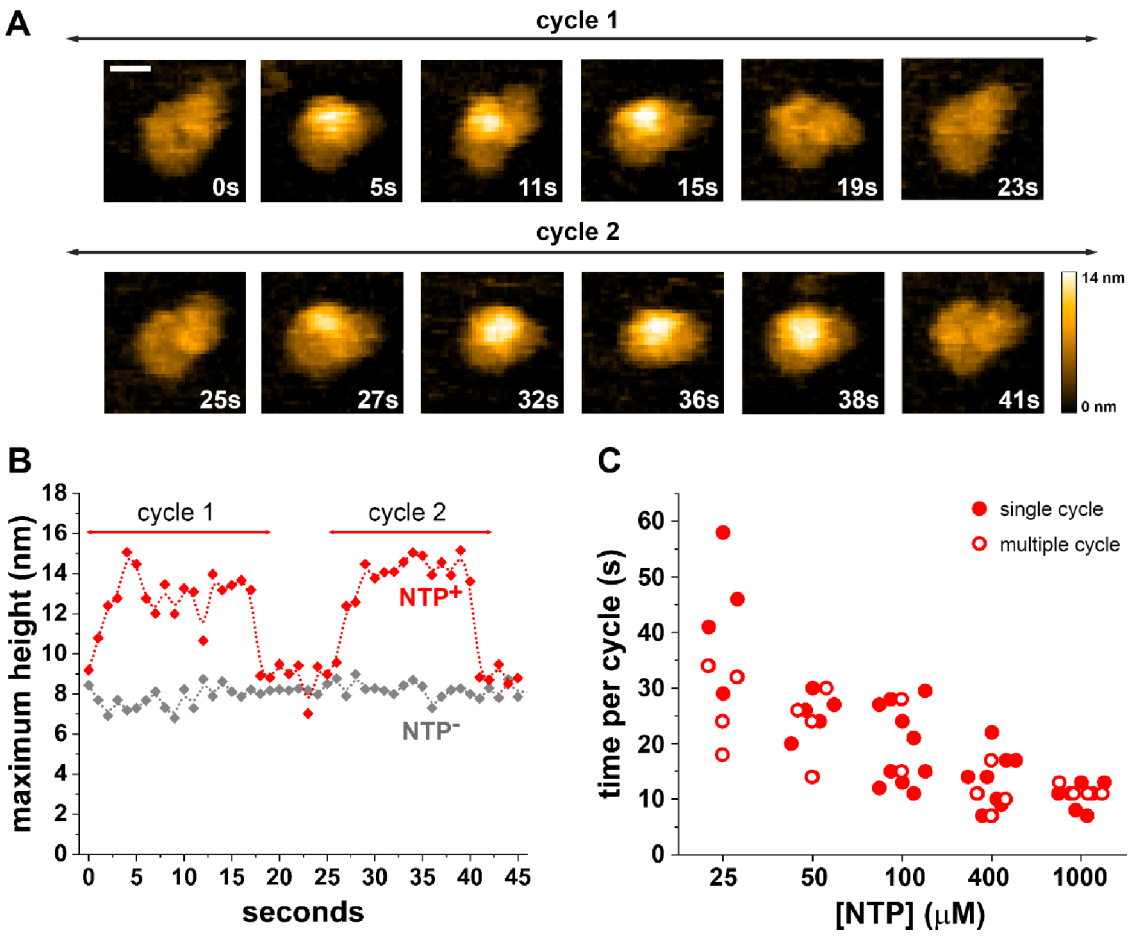

Figure 4. Consecutive rounds of RNA synthesis by individual rRNPs. (A) Successive HS-AFM video frames of a representative rRNP undergoing two consecutive conformational cycles (cycle 1 and cycle 2) of similar durations under conditions compatible with RNA synthesis (ApG 100 μM, NTPs 50 μM), Supplementary Video 11 (1 fps); scale bar = 20 nm. Additional HS-AFM videos of consecutive conformational cycles are shown in Supplementary Video 12. (B) Red symbols show the variation of the maximum height over time of the rRNP shown in A. The two conformational cycles are observed as consecutive periods of increased maximum height. As indicated in the main text, 16% (N = 21) of the active rRNPs imaged in this study (N = 134) went through consecutive conformational cycles. In contrast, no significant changes in the maximum height of rRNPs were observed in the absence of NTPs (gray symbols). (C) Time to complete a single conformational cycle as a function of NTP concentration for rRNPs that undergo one cycle (filled red symbols) compared with rRNPs that complete several consecutive cycles (empty red symbols).

direct experimental evidence of the ability of the RdRp to undergo consecutive rounds of RNA synthesis within the RNP context.

The rRNP conformational cycle revealed by our studies can be interpreted in light of models previously proposed for the vRNP transcription cycle (Figure 1F and Supplementary Animation 1).[5,11] Recent cryo-EM-based studies of actively transcribing native IAV vRNPs showed that the RdRp carries out transcription attached to the two ends of the NP/RNA template and without disrupting the overall double-helical structure of the vRNP complex (processive helical track model).[5] Later structural studies on active RdRp bound to a short RNA fragment provided a detailed picture of the intricate conformational changes of the template and RdRp structures required to ensure transcription without losing the two ends of the template.[11] According to these works, during transcription elongation, advancement of the RdRp along the template holding its two ends would promote the formation of two template loops on either side of the polymerase; one loop would correspond to the incoming template, and the other to the outgoing template. In agreement with this prediction, the characteristic annular organization of rRNPs allowed for clear visualization of the formation of template loops during RNA synthesis. Classification and 2D averaging of HS-AFM video frames and EM images of conformational states of rRNPs stalled during RNA synthesis showed the accumulation of bowtie-like structures with two loops protruding from a central mass (Figure 2C–E). In these images, the central mass would correspond to the position of the polymerase, and the loops to the incoming and outgoing RNA/NP template, which would shrink and grow, respectively, as RNA synthesis proceeds. In fact, the stalled conformations identified in this work present loops of different sizes, suggesting that they correspond to rRNPs in different stages of RNA synthesis.

During transcription elongation, each NP was transiently peeled off the vRNA template. This is because the active site of the RdRp binds roughly the same amount of vRNA that can bind to one NP (~25 nt).[9−11,35] Daisy-chain NP−NP interactions would prevent NP release, while transient interactions between the peeled NP and a putative NP docking site at the polymerase surface would hold the NP in place for rebinding to the outgoing vRNA template.[4,11,21,36]

https://doi.org/10.1021/acsnano.4c01362
ACS Nano 2024, 18, 19518−19527

Interestingly, HS-AFM imaging revealed that the conformational transitions of the rRNP during RNA synthesis were always accompanied by a local increase in the height of the complex, which was compatible with the superposition of the heights of RdRp and a single NP protein. This observation supports the idea that local transient interactions could be stabilized between the two proteins during the elongation phase of RNA synthesis (Figure 1F and Supplementary Animation 1) and interactions that may occur at the hypothesized polymerase-NP docking site.

Several lines of evidence have implied that single vRNPs can perform several rounds of RNA synthesis or transcription: vRNPs preserve their overall structure during transcription;[5] transcription does not require additional viral components;[37] and viral mRNA accumulates in the presence of the translational inhibitor cycloheximide.[38] Our HS-AFM experiments showed that a significant number of rRNPs performed consecutive cycles of RNA synthesis within our observational time window. This result demonstrates their ability to recycle while maintaining both their structural and functional integrity during the RNA synthesis cycle. This recycling capability would enable each individual vRNP to produce multiple copies of mRNA and is therefore essential for efficient viral multiplication.

Knowing the average duration of the conformational cycle allowed us to estimate the average rate of RNA synthesis in rRNPs at NTP concentrations > 400 μM to be approximately 30 nt/s. This value is consistent with the average rates of the elongation phase of transcription for other DNA- and RNA-dependent RNA polymerases studied *in singulo* at saturating NTP conditions and room temperature, which range from 10 to 30 nt/s.[30,39−41] According to this result, native vRNPs would transcribe the longest IAV genome segments (e.g., PB1; 2200 nt) within approximately 1 min. Although conditions *in vivo* would vary, the relatively fast average synthesis rates of the RNPs and their ability to recycle measured in this work predict that individual vRNPs of IAV would be capable of producing multiple copies of mRNA in the early stages of infection.[42,43]

In addition, our results showed the effect on average RNA synthesis rate caused by incorporation of UTP analogs into the nascent RNA that altered the stability of the RNA secondary structure. Incorporation of $m^1\Psi$, which stabilizes the secondary structure of RNA by increasing the average base pairing energy by 0.18 kcal/mol relative to UTP,[34] decreased the average RNA synthesis rate by ∼15% at saturating nucleotide concentrations (≥400 μM). On the other hand, incorporation of mo^5U, which decreases the base pairing energy by 0.28 kcal/mol relative to UTP,[34] increased the average RNA synthesis rate of the rRNP by up to 2 times at all NTP concentrations tested. These results argue that the stability of the secondary structure of the nascent RNA modulates the average replication rate of the RdRp. In particular, our results are consistent with the fact that a less-structured nascent RNA is beneficial for the RNA synthesis rate of IAV RdRp within the context of the RNP. This observation is in line with the well-known effect of co-transcriptional folding on regulating the average transcription rates of DNA-dependent RNA polymerases.[29] In particular, formation of secondary structure in the nascent RNA modulates the propensity of the polymerase to enter and exit pause states during transcript elongation.[30] Taken together, our data strongly suggest that nascent RNA with a less stable secondary structure would increase the average RNA synthesis rate of the RdRp by decreasing its pause occupancy.

CONCLUSIONS

Annular rRNPs serve as an optimal model system for monitoring the conformational dynamics of the NP-RNA template during RNA synthesis with HS-AFM. Moreover, this technique allows us to track the activity of one rRNP at a time, providing information about the kinetics of the RNA synthesis reaction that is unattainable with other methods. For instance, transcriptional pausing is an intrinsic property of most RNA polymerases, and its regulation constitutes one of the central mechanisms of control of gene expression.[44] Future single-molecule experiments of real-time RNA synthesis kinetics by the IAV RdRp within the context of the RNP will help to elucidate the nature of putative pause states and their roles in viral transcription and replication.

EXPERIMENTAL SECTION

Production, Purification, and Functional Characterization of rRNPs. rRNPs carrying a 352-nt fragment of IAV NS protein genomic RNA (Supporting Information (SI) Figure S1A) were produced, amplified *in vivo*, and purified following previously described methods (SI).[9,22] Fractions from the purified rRNP were assayed for *in vitro* transcriptional activity as described in Figure S1B.

HS-AFM Imaging and Analysis. A custom-built HS-AFM apparatus[45,46] was used to scan the samples in liquid using the tapping mode. The free-oscillation amplitude of the cantilever (A_0) was set to ∼2 nm, and the set point of the feedback amplitude was set to ∼0.9 × Å. To reduce the tapping force, a recently developed "only trace imaging" mode was employed in several observations.[47] A glass stage (Japan Cell Co., Ltd., Japan; 1.5 mm in diameter and 2 mm in height) with a mica disc (Furuuchi Chemical Corp., Japan; 1.5 mm in diameter and 0.05 mm in thickness) was attached to the top of the Z-scanner by using nail polish. Cantilevers (BL-AC10DS-A2, Olympus, Japan) with a spring constant of ∼0.15 N/m, resonance frequency of ∼500 kHz in water, and quality factor of ∼1.5 in water were used. The detailed procedures of HS-AFM measurement and tip preparation are described elsewhere and in the SI Methods section.[48]

rRNPs were diluted in the reaction or imaging buffer (50 mM Tris-HCl [pH 8.0], 2 mM $MgCl_2$, 100 mM KCl, and 1 mM DTT) containing 100 μM ApG (TriLink BioTechnologies Inc., USA) and the indicated concentrations of NTP or NTP−uridine analogue mixtures (TriLink BioTechnologies Inc., USA). After incubation for 15 min at 30 °C, 2 μL of the mixture was deposited on a freshly cleaved mica surface; after 3 min incubation in a humid chamber, the sample on the stage was rinsed with imaging buffer. Measurements were performed at 25 °C after adding ApG (100 μM) and the indicated concentrations of NTP or NTP−uridine analogue mixtures to the imaging buffer (SI).

To obtain two-dimensional (2D) averages from the HS-AFM data, the corresponding video frames were converted to mrc image format using BSOFT software.[49] These frames were imported as particle images in Scipion[50] and treated as analogous to EM data except that contrast transfer function (CTF) estimation was not applied in this case. To produce the 2D averages, images were subjected to an unsupervised 2D classification using the CL2D algorithm[51] as implemented in Scipion software.

The average RNA synthesis rate within the context of the rRNP was estimated by dividing the template length (352 nt) by the time required to accomplish a full conformational cycle. Events 6 times longer or shorter than the average were discarded since they may correspond to inactivated molecules or failure of RNA synthesis initiation.

Electron Microscopy Imaging and Analysis. For the analysis of RNA synthesis with negative staining EM, rRNPs were incubated in the reaction buffer containing 1 U/μL RNasin, 100 μM ApG, 1

https://doi.org/10.1021/acsnano.4c01362
ACS Nano 2024, 18, 19518−19527

mM NTPs, and 12.5 μM of the nonhydrolyzable nucleotide analogue UpNHpp (ratio UTP:UpNHpp 80:1) at 30 °C for 3 h. After incubation, samples were applied to carbon-coated grids and visualized in a JEOL 1400 Flash electron microscope (SI Methods). For image processing, operations were carried out using the Xmipp[52,53] and RELION[54] processing packages within the Scipion platform (http://scipion.i2pc.es/[50]). Further details of image processing are described in the SI Methods section.

ASSOCIATED CONTENT

Supporting Information

The Supporting Information is available free of charge at https://pubs.acs.org/doi/10.1021/acsnano.4c01362.

Supplementary methods; supplementary figures of *in vitro* RNA synthesis assays; HS-AFM images of native and recombinant vRNPs; nascent RNA secondary structure prediction; supplementary references (PDF)

Supplementary video 1. HS-AFM video of a single rRNP in the reaction buffer without NTPs (AVI)

Supplementary video 2. Mosaic of 3 additional HS-AFM videos of independent rRNPs in the reaction buffer without NTPs (MP4)

Supplementary video 3. Conformational changes of a single rRNP in the presence of ApG/NTPs (AVI)

Supplementary video 4. The conformational change of the rRNPs is halted in the presence of UpNHpp (AVI)

Supplementary video 5. Conformational cycle at 25 μM NTP concentration (AVI)

Supplementary video 6. Conformational cycle at 50 μM NTP concentration (AVI)

Supplementary video 7. Conformational cycle at 400 μM NTP concentration (AVI)

Supplementary video 8. Mosaic of 6 additional HS-AFM videos of independent rRNPs in the reaction buffer containing NTPs (AVI)

Supplementary video 9. Mosaic of 6 HS-AFM videos of independent rRNPs in the reaction buffer containing mo5U/ NTP(AVI)

Supplementary video 10. Mosaic of 6 HS-AFM videos of independent rRNPs in the reaction buffer containing $m^1\Psi$ NTP (AVI)

Supplementary video 11. Consecutive conformational cycles of individual rRNPs during RNA synthesis (AVI)

Supplementary video 12. Mosaic of 3 additional HS-AFM videos of independent rRNPs undergoing consecutive conformational cycles (MP4)

Supplementary Animation 1 (MP4)

AUTHOR INFORMATION

Corresponding Authors

Shingo Fukuda − *WPI Nano Life Science Institute (WPI-NanoLSI), Kanazawa University, Kakuma-machi, Kanazawa 920-1192, Japan;* orcid.org/0000-0002-0723-2088; Email: shingofukuda@staff.kanazawa-u.ac.jp

Jaime Martin-Benito − *IMDEA Nanociencia & CNB-CSIC-IMDEA Nanociencia Associated Unit "Unidad de Nanobiotecnología", 28049 Madrid, Spain;* Email: jmartinb@cnb.csic.es

Borja Ibarra − *Instituto Madrileño de Estudios Avanzados en Nanociencia, IMDEA Nanociencia, 28049 Madrid, Spain; IMDEA Nanociencia & CNB-CSIC-IMDEA Nanociencia Associated Unit "Unidad de Nanobiotecnología", 28049 Madrid, Spain;* orcid.org/0000-0001-6597-797X; Email: borja.ibarra@imdea.org

Authors

Diego Carlero − *Centro Nacional de Biotecnología Campus de Cantoblanco, 28049 Madrid, Spain*

Rebeca Bocanegra − *Instituto Madrileño de Estudios Avanzados en Nanociencia, IMDEA Nanociencia, 28049 Madrid, Spain; IMDEA Nanociencia & CNB-CSIC-IMDEA Nanociencia Associated Unit "Unidad de Nanobiotecnología", 28049 Madrid, Spain*

Toshio Ando − *WPI Nano Life Science Institute (WPI-NanoLSI), Kanazawa University, Kakuma-machi, Kanazawa 920-1192, Japan;* orcid.org/0000-0001-8819-154X

Complete contact information is available at: https://pubs.acs.org/10.1021/acsnano.4c01362

Author Contributions

¶D.C., S.F., and R.B. contributed equally to this work.

Notes

The authors declare no competing financial interest.

ACKNOWLEDGMENTS

This work was supported by the NanoLSI Visiting Fellows Program 2019 (to B.I.), the World Premier International Research Center Initiative (WPI), MEXT (Japan), and grants PGC2018-099341-B-I00 (to B.I.), PID2021-126755NB-I00 (to B.I.), and PID2020-117752RB-I00 (to J.M.B.) financed by MCIU/AEI/10.13039/501100011033 and FEDER, UE, Grant TED2021-132748B-I00 financed by the European Union "NextGeneration EU"/PRTR (to J.M.B.), and Grant No. 20K15140 financed by JSPS KAKENHI (to S.F.). IMDEA Nanociencia acknowledges support from the Severo Ochoa Program for Centers of Excellence in R&D (CEX2020-001039-S).

REFERENCES

(1) Neumann, G.; Brownlee, G. G.; Fodor, E.; Kawaoka, Y. *Orthomyxovirus Replication, Transcription, and Polyadenylation* **2004**, *283*, 121−143.

(2) Compans, R. W.; Content, J.; Duesberg, P. H. Structure of the Ribonucleoprotein of Influenza Virus. *J. Virol* **1972**, *10* (4), 795−800.

(3) Pons, M. W.; Schulze, I. T.; Hirst, G. K. Isolation and Characterization of the Ribonucleoprotein of Influenza Virus. *Virology* **1969**, *39* (2), 250−259.

(4) Arranz, R.; Coloma, R.; Chichón, F. J.; Conesa, J. J.; Carrascosa, J. L.; Valpuesta, J. M.; Ortín, J.; Martín-Benito, J. The Structure of Native Influenza Virion Ribonucleoproteins. *Science* **2012**, *338*, 1634.

(5) Coloma, R.; Arranz, R.; de la Rosa-Trevín, J. M.; Sorzano, C. O. S.; Munier, S.; Carlero, D.; Naffakh, N.; Ortín, J.; Martín-Benito, J. Structural Insights into Influenza A Virus Ribonucleoproteins Reveal a Processive Helical Track as Transcription Mechanism. *Nat. Microbiol* **2020**, *5* (5), 727−734.

(6) Hay, A. J.; Lomniczi, B.; Bellamy, A. R.; Skehel, J. J. Transcription of the Influenza Virus Genome. *Virology* **1977**, *83* (2), 337−355.

(7) Hsu, M. T.; Parvin, J. D.; Gupta, S.; Krystal, M.; Palese, P. Genomic RNAs of Influenza Viruses Are Held in a Circular Conformation in Virions and in Infected Cells by a Terminal Panhandle. *Proc. Natl. Acad. Sci. U. S. A.* **1987**, *84* (22), 8140−8144.

(8) Fodor, E.; Seong, B. L.; Brownlee, G. G. Photochemical Cross-Linking of Influenza A Polymerase to Its Virion RNA Promoter Defines a Polymerase Binding Site at Residues 9 to 12 of the Promoter. *Journal of General Virology* **1993**, *74* (7), 1327−1333.

(9) Ortega, J.; Martín-Benito, J.; Zürcher, T.; Valpuesta, J. M.; Carrascosa, J. L.; Ortín, J. Ultrastructural and Functional Analyses of Recombinant Influenza Virus Ribonucleoproteins Suggest Dimerization of Nucleoprotein during Virus Amplification. *J. Virol* **2000**, *74* (1), 156−163.
(10) Kouba, T.; Drncová, P.; Cusack, S. Structural Snapshots of Actively Transcribing Influenza Polymerase. *Nat. Struct Mol. Biol.* **2019**, *26* (6), 460−470.
(11) Wandzik, J. M.; Kouba, T.; Karuppasamy, M.; Pflug, A.; Drncova, P.; Provaznik, J.; Azevedo, N.; Cusack, S. A Structure-Based Model for the Complete Transcription Cycle of Influenza Polymerase. *Cell* **2020**, *181* (4), 877−893.
(12) Pflug, A.; Guilligay, D.; Reich, S.; Cusack, S. Structure of Influenza A Polymerase Bound to the Viral RNA Promoter. *Nature* **2014**, *516* (7531), 355−360.
(13) Lukarska, M.; Fournier, G.; Pflug, A.; Resa-Infante, P.; Reich, S.; Naffakh, N.; Cusack, S. Structural Basis of an Essential Interaction between Influenza Polymerase and Pol II CTD. *Nature* **2017**, *541*, 117.
(14) Pflug, A.; Gaudon, S.; Resa-Infante, P.; Lethier, M.; Reich, S.; Schulze, W. M.; Cusack, S. Capped RNA Primer Binding to Influenza Polymerase and Implications for the Mechanism of Cap-Binding Inhibitors. *Nucleic Acids Res.* **2018**, *46*, 956.
(15) Chiaruttini, N.; Redondo-Morata, L.; Colom, A.; Humbert, F.; Lenz, M.; Scheuring, S.; Roux, A. Relaxation of Loaded ESCRT-III Spiral Springs Drives Membrane Deformation. *Cell* **2015**, *163* (4), 866−879.
(16) Miyagi, A.; Ramm, B.; Schwille, P.; Scheuring, S. High-Speed Atomic Force Microscopy Reveals the Inner Workings of the MinDE Protein Oscillator. *Nano Lett.* **2018**, *18* (1), 288−296.
(17) Kodera, N.; Yamamoto, D.; Ishikawa, R.; Ando, T. Video Imaging of Walking Myosin V by High-Speed Atomic Force Microscopy. *Nature* **2010**, *468* (7320), 72−76.
(18) Ando, T.; Uchihashi, T.; Scheuring, S. Filming Biomolecular Processes by High-Speed Atomic Force Microscopy. *Chem. Rev.* **2014**, *114* (6), 3120−3188.
(19) Casuso, I.; Redondo-Morata, L.; Rico, F. Biological Physics by High-Speed Atomic Force Microscopy. *Philosophical Transactions of the Royal Society A: Mathematical, Physical and Engineering Sciences* **2020**, *378* (2186), 20190604.
(20) Nievergelt, A. P.; Banterle, N.; Andany, S. H.; Gönczy, P.; Fantner, G. E. High-Speed Photothermal off-Resonance Atomic Force Microscopy Reveals Assembly Routes of Centriolar Scaffold Protein SAS-6. *Nat. Nanotechnol* **2018**, *13* (8), 696−701.
(21) Martín-Benito, J.; Area, E.; Ortega, J.; Llorca, O.; Valpuesta, J. M.; Carrascosa, J. L.; Ortín, J. Three-dimensional Reconstruction of a Recombinant Influenza Virus Ribonucleoprotein Particle. *EMBO Rep* **2001**, *2* (4), 313−317.
(22) Coloma, R.; Valpuesta, J. M.; Arranz, R.; Carrascosa, J. L.; Ortín, J.; Martín-Benito, J. The Structure of a Biologically Active Influenza Virus Ribonucleoprotein Complex. *PLoS Pathog* **2009**, *5* (6), No. e1000491.
(23) Area, E.; Martín-Benito, J.; Gastaminza, P.; Torreira, E.; Valpuesta, J. M.; Carrascosa, J. L.; Ortín, J. 3D Structure of the Influenza Virus Polymerase Complex: Localization of Subunit Domains. *Proc. Natl. Acad. Sci. U. S. A.* **2004**, *101* (1), 308−313.
(24) Reich, S.; Guilligay, D.; Pflug, A.; Malet, H.; Berger, I.; Crépin, T.; Hart, D.; Lunardi, T.; Nanao, M.; Ruigrok, R. W. H.; Cusack, S. Structural Insight into Cap-Snatching and RNA Synthesis by Influenza Polymerase. *Nature* **2014**, *516* (7531), 361−366.
(25) Plotch, S. J.; Krug, R. M. Influenza Virion Transcriptase: Synthesis in Vitro of Large, Polyadenylic Acid-Containing Complementary RNA. *J. Virol* **1977**, *21* (1), 24−34.
(26) McGeoch, D.; Kitron, N. Influenza Virion RNA-Dependent RNA Polymerase: Stimulation by Guanosine and Related Compounds. *J. Virol* **1975**, *15* (4), 686−695.
(27) Dangkulwanich, M.; Ishibashi, T.; Liu, S.; Kireeva, M. L.; Lubkowska, L.; Kashlev, M.; Bustamante, C. J. Complete Dissection of Transcription Elongation Reveals Slow Translocation of RNA Polymerase II in a Linear Ratchet Mechanism. *Elife* **2013**, *2*, DOI: 10.7554/eLife.00971.
(28) Wang, B.; Sexton, R. E.; Feig, M. Kinetics of Nucleotide Entry into RNA Polymerase Active Site Provides Mechanism for Efficiency and Fidelity. *Biochimica et Biophysica Acta (BBA) - Gene Regulatory Mechanisms* **2017**, *1860* (4), 482−490.
(29) Schärfen, L.; Neugebauer, K. M. Transcription Regulation Through Nascent RNA Folding. *J. Mol. Biol.* **2021**, *433* (14), 166975.
(30) Zamft, B.; Bintu, L.; Ishibashi, T.; Bustamante, C. Nascent RNA Structure Modulates the Transcriptional Dynamics of RNA Polymerases. *Proc. Natl. Acad. Sci. U. S. A.* **2012**, *109* (23), 8948−8953.
(31) Turowski, T. W.; Petfalski, E.; Goddard, B. D.; French, S. L.; Helwak, A.; Tollervey, D. Nascent Transcript Folding Plays a Major Role in Determining RNA Polymerase Elongation Rates. *Mol. Cell* **2020**, *79* (3), 488−503.
(32) Saldi, T.; Riemondy, K.; Erickson, B.; Bentley, D. L. Alternative RNA Structures Formed during Transcription Depend on Elongation Rate and Modify RNA Processing. *Mol. Cell* **2021**, *81* (8), 1789−1801.
(33) Markham, N. R.; Zuker, M. *UNAFold* **2008**, *453*, 3−31.
(34) Mauger, D. M.; Cabral, B. J.; Presnyak, V.; Su, S. V.; Reid, D. W.; Goodman, B.; Link, K.; Khatwani, N.; Reynders, J.; Moore, M. J.; McFadyen, I. J. MRNA Structure Regulates Protein Expression through Changes in Functional Half-Life. *Proc. Natl. Acad. Sci. U. S. A.* **2019**, *116* (48), 24075−24083.
(35) Hutchinson, E. C.; Charles, P. D.; Hester, S. S.; Thomas, B.; Trudgian, D.; Martínez-Alonso, M.; Fodor, E. Conserved and Host-Specific Features of Influenza Virion Architecture. *Nat. Commun.* **2014**, *5* (1), 4816.
(36) Ye, Q.; Krug, R. M.; Tao, Y. J. The Mechanism by Which Influenza A Virus Nucleoprotein Forms Oligomers and Binds RNA. *Nature* **2006**, *444* (7122), 1078−1082.
(37) Jorba, N.; Coloma, R.; Ortín, J. Genetic Trans-Complementation Establishes a New Model for Influenza Virus RNA Transcription and Replication. *PLoS Pathog* **2009**, *5* (5), No. e1000462.
(38) Vreede, F. T.; Jung, T. E.; Brownlee, G. G. Model Suggesting That Replication of Influenza Virus Is Regulated by Stabilization of Replicative Intermediates. *J. Virol* **2004**, *78* (17), 9568−9572.
(39) Dulin, D.; Vilfan, I. D.; Berghuis, B. A.; Hage, S.; Bamford, D. H.; Poranen, M. M.; Depken, M.; Dekker, N. H. Elongation-Competent Pauses Govern the Fidelity of a Viral RNA-Dependent RNA Polymerase. *Cell Rep* **2015**, *10* (6), 983−992.
(40) Neuman, K. C.; Abbondanzieri, E. A.; Landick, R.; Gelles, J.; Block, S. M. Ubiquitous Transcriptional Pausing Is Independent of RNA Polymerase Backtracking. *Cell* **2003**, *115* (4), 437−447.
(41) Duss, O.; Stepanyuk, G. A.; Grot, A.; O'Leary, S. E.; Puglisi, J. D.; Williamson, J. R. Real-Time Assembly of Ribonucleoprotein Complexes on Nascent RNA Transcripts. *Nat. Commun.* **2018**, *9* (1), 5087.
(42) Hatada, E.; Hasegawa, M.; Mukaigawa, J.; Shimizu, K.; Fukuda, R. Control of Influenza Virus Gene Expression: Quantitative Analysis of Each Viral RNA Species in Infected Cells. *Journal of Biochemistry* **1989**, *105* (4), 537−546.
(43) Russell, A. B.; Trapnell, C.; Bloom, J. D. Extreme Heterogeneity of Influenza Virus Infection in Single Cells. *Elife* **2018**, *7*, DOI: 10.7554/eLife.32303.
(44) Landick, R. Transcriptional Pausing as a Mediator of Bacterial Gene Regulation. *Annu. Rev. Microbiol.* **2021**, *75* (1), 291−314.
(45) Ando, T.; Kodera, N.; Takai, E.; Maruyama, D.; Saito, K.; Toda, A. A High-Speed Atomic Force Microscope for Studying Biological Macromolecules. *Proc. Natl. Acad. Sci. U. S. A.* **2001**, *98* (22), 12468−12472.
(46) Ando, T.; Uchihashi, T.; Fukuma, T. High-Speed Atomic Force Microscopy for Nano-Visualization of Dynamic Biomolecular Processes. *Prog. Surf. Sci.* **2008**, *83* (7−9), 337−437.
(47) Fukuda, S.; Ando, T. Faster High-Speed Atomic Force Microscopy for Imaging of Biomolecular Processes. *Rev. Sci. Instrum.* **2021**, *92*(3), 033705, DOI: 10.1063/5.0032948.

(48) Uchihashi, T.; Kodera, N.; Ando, T. Guide to Video Recording of Structure Dynamics and Dynamic Processes of Proteins by High-Speed Atomic Force Microscopy. *Nat. Protoc.* **2012**, *7* (6), 1193−1206.
(49) Heymann, J. B. Bsoft: Image and Molecular Processing in Electron Microscopy. *J. Struct Biol.* **2001**, *133* (2−3), 156−169.
(50) de la Rosa-Trevín, J. M.; Quintana, A.; del Cano, L.; Zaldívar, A.; Foche, I.; Gutiérrez, J.; Gómez-Blanco, J.; Burguet-Castell, J.; Cuenca-Alba, J.; Abrishami, V.; Vargas, J.; Otón, J.; Sharov, G.; Vilas, J. L.; Navas, J.; Conesa, P.; Kazemi, M.; Marabini, R.; Sorzano, C. O. S.; Carazo, J. M. Scipion: A Software Framework toward Integration, Reproducibility and Validation in 3D Electron Microscopy. *J. Struct Biol.* **2016**, *195* (1), 93−99.
(51) Sorzano, C. O. S.; Bilbao-Castro, J. R.; Shkolnisky, Y.; Alcorlo, M.; Melero, R.; Caffarena-Fernández, G.; Li, M.; Xu, G.; Marabini, R.; Carazo, J. M. A Clustering Approach to Multireference Alignment of Single-Particle Projections in Electron Microscopy. *J. Struct Biol.* **2010**, *171* (2), 197−206.
(52) de la Rosa-Trevín, J. M.; Otón, J.; Marabini, R.; Zaldívar, A.; Vargas, J.; Carazo, J. M.; Sorzano, C. O. S. Xmipp 3.0: An Improved Software Suite for Image Processing in Electron Microscopy. *J. Struct Biol.* **2013**, *184* (2), 321−328.
(53) Scheres, S. H. W.; Núñez-Ramírez, R.; Sorzano, C. O. S.; Carazo, J. M.; Marabini, R. Image Processing for Electron Microscopy Single-Particle Analysis Using XMIPP. *Nat. Protoc* **2008**, *3* (6), 977−990.
(54) Scheres, S. H. W. RELION: Implementation of a Bayesian Approach to Cryo-EM Structure Determination. *J. Struct Biol.* **2012**, *180* (3), 519−530.

https://doi.org/10.1021/acsnano.4c01362
ACS Nano 2024, 18, 19518−19527